



**HAL**  
open science

**Corrigendum to “Pyrite iron isotope compositions track local sedimentation conditions through the Smithian-Spathian transition (Early Triassic, Utah, USA)” [Palaeogeography, Palaeoclimatology, Palaeoecology, 617 (2023), 1–16].**

Marie-Noëlle Decraene, Johanna Marin-Carbonne, Christophe Thomazo, Arnaud Brayard, Anne-Sophie Bouvier, Brahimsamba Bomou, Thierry Adatte, Nicolas Olivier

► **To cite this version:**

Marie-Noëlle Decraene, Johanna Marin-Carbonne, Christophe Thomazo, Arnaud Brayard, Anne-Sophie Bouvier, et al.. Corrigendum to “Pyrite iron isotope compositions track local sedimentation conditions through the Smithian-Spathian transition (Early Triassic, Utah, USA)” [Palaeogeography, Palaeoclimatology, Palaeoecology, 617 (2023), 1–16].. Palaeogeography, Palaeoclimatology, Palaeoecology, 2023, 623, pp.111636. 10.1016/j.palaeo.2023.111636 . hal-04156093

**HAL Id: hal-04156093**

**<https://u-bourgogne.hal.science/hal-04156093>**

Submitted on 19 Oct 2023

**HAL** is a multi-disciplinary open access archive for the deposit and dissemination of scientific research documents, whether they are published or not. The documents may come from teaching and research institutions in France or abroad, or from public or private research centers.

L'archive ouverte pluridisciplinaire **HAL**, est destinée au dépôt et à la diffusion de documents scientifiques de niveau recherche, publiés ou non, émanant des établissements d'enseignement et de recherche français ou étrangers, des laboratoires publics ou privés.



## Corrigendum to “Pyrite iron isotope compositions track local sedimentation conditions through the Smithian-Spathian transition (Early Triassic, Utah, USA)” [Palaeogeography, Palaeoclimatology, Palaeoecology, 617 (2023), 1–16]

Marie-Noëlle Decraene<sup>a,\*</sup>, Johanna Marin-Carbonne<sup>a</sup>, Christophe Thomazo<sup>b,c</sup>, Arnaud Brayard<sup>b</sup>, Anne-Sophie Bouvier<sup>a</sup>, Brahimsamba Bomou<sup>a</sup>, Thierry Adatte<sup>a</sup>, Nicolas Olivier<sup>d</sup>

<sup>a</sup> Institut des Sciences de la Terre, Université de Lausanne, Lausanne, Switzerland

<sup>b</sup> Biogéosciences, UMR6282, CNRS, Université Bourgogne, 6 Boulevard Gabriel, 21000 Dijon, France

<sup>c</sup> Institut Universitaire de France

<sup>d</sup> Université Clermont Auvergne, CNRS, IRD, Laboratoire Magmas et Volcans, F-63000 Clermont-Ferrand, France

Balmat pyrite standard (Whitehouse and Fedo, 2007; Marin-Carbonne et al., 2011) is known to have variable  $\delta^{56}\text{Fe}$  values (Xu et al., 2022). We have recently reanalyzed the batch of Balmat standard from UNIL (hereafter called Balmat-UNIL) at the University of Chicago (courtesy of Dr. Rego and Prof. Dauphas, unpublished data). The  $\delta^{56}\text{Fe}$  bulk value of Balmat-UNIL pyrite used in this study is  $-1.459 \pm 0.024$  ‰, compared to the previous published value of  $-0.399$  ‰ (Whitehouse and Fedo, 2007). As all the SIMS data are standardized to the Balmat-UNIL pyrite, the correction with this new value led to a shift of 1.06 ‰ of the entire published dataset. This corrigendum presents the corrected pyrite Fe isotope data, now displaying variations between  $-3.05$  ‰ and  $+4.33$  ‰. Most of the figures (Figs. 3, 4, 6, 7, 8, 9, 10 and 11), and the supplementary data (Figs. S3, S5, S6 and Table S9) need to be modified as presented below. As a result of this shift, we also propose hereafter an alternative model to explain the  $\delta^{56}\text{Fe}$  signal of pyrite precipitated in the inner ramp system (section 4.3.1 - discussion), combining petrographic observations and both pyrite S and newly corrected Fe isotope results.

The authors would like to apologize for this mistake.

*Revised model for pyrite formation in the inner ramp system (section 4.3.1 and Fig. 10):*

The LWC inner ramp is characterized by frequent sediment remobilization by physical reworking (tidal currents or waves) and bioturbation, which facilitated the connection between sediment porewaters and the overlying water column. Therefore, sulfates, Fe-oxides and organic matter that fuel metabolic reactions related to sedimentary sulfides precipitation are assumed to be non-limiting. An open system is consistent with the average negative  $\delta^{34}\text{S}$  value recorded

in the inner ramp samples ( $\delta^{34}\text{S} = -11.4 \pm 9.3$  ‰, 1SD) and specifically in samples LWC31, LWC39 and LWC41, with values lower than  $-16.8$  ‰. The model described in the original version of this article may still explain the variability of Fe isotope compositions in FA1 and FA2 samples of the inner ramp system, assuming that the  $\delta^{56}\text{Fe}$  value of the Fe source is close to 0 ‰. Such iron isotopic signal can be derived, for example, from quantitative iron oxidation into  $\text{Fe}^{3+}$ -minerals after weathering of igneous rocks, aerosols, or river loads (Dauphas and Rouxel, 2006 for a review). However, the Fe isotope compositions in FA1 and FA2 samples may also be alternatively interpreted, assuming that the  $\delta^{56}\text{Fe}$  value of the initial Fe oxides is close to the canonical Fe isotope composition of  $+0.9$  ‰ known for Fe oxides throughout Earth history (Rouxel et al., 2005; Wu et al., 2011; corrected Fig. 10). In that case, the Fe isotope variability measured in pyrite grains from the inner ramp would be primarily controlled by the availability of microbially-produced  $\text{H}_2\text{S}$  (corrected Fig. 10). Through this alternative model, the average  $\delta^{56}\text{Fe}$  value of  $+0.97$  ‰ (1SD) associated with FA2 (MISS) samples would reflect the complete sulfidation of Fe-oxides, allowing the preservation of the initial  $\delta^{56}\text{Fe}$  value of Fe-oxides within pyrite (corrected Fig. 10a and c). This process can be supported by  $\text{H}_2\text{S}$  production in biofilms after microbial sulfate reduction (MSR). Consequently, in sediments devoid of biofilms (FA1, siltstones), the sulfidation of Fe-oxides may be limited by lower production rates of  $\text{H}_2\text{S}$  by sulfate reducers, related to a lower reactivity of organic compounds (corrected Fig. 10b). Indeed, under well-ventilated conditions, MSR occurs deeper in the sediments where the quantity and reactivity of organic matter decrease as a function of the sediment depth and redox potential (Middelburg, 1989; Dauwe et al., 1999; Meister et al., 2013). Although

DOI of original article: <https://doi.org/10.1016/j.palaeo.2023.111507>.

\* Corresponding author.

E-mail address: [marie-noelle.decraene@unil.ch](mailto:marie-noelle.decraene@unil.ch) (M.-N. Decraene).

<https://doi.org/10.1016/j.palaeo.2023.111636>

Available online 20 May 2023

0031-0182/© 2023 The Author(s). Published by Elsevier B.V. All rights reserved.

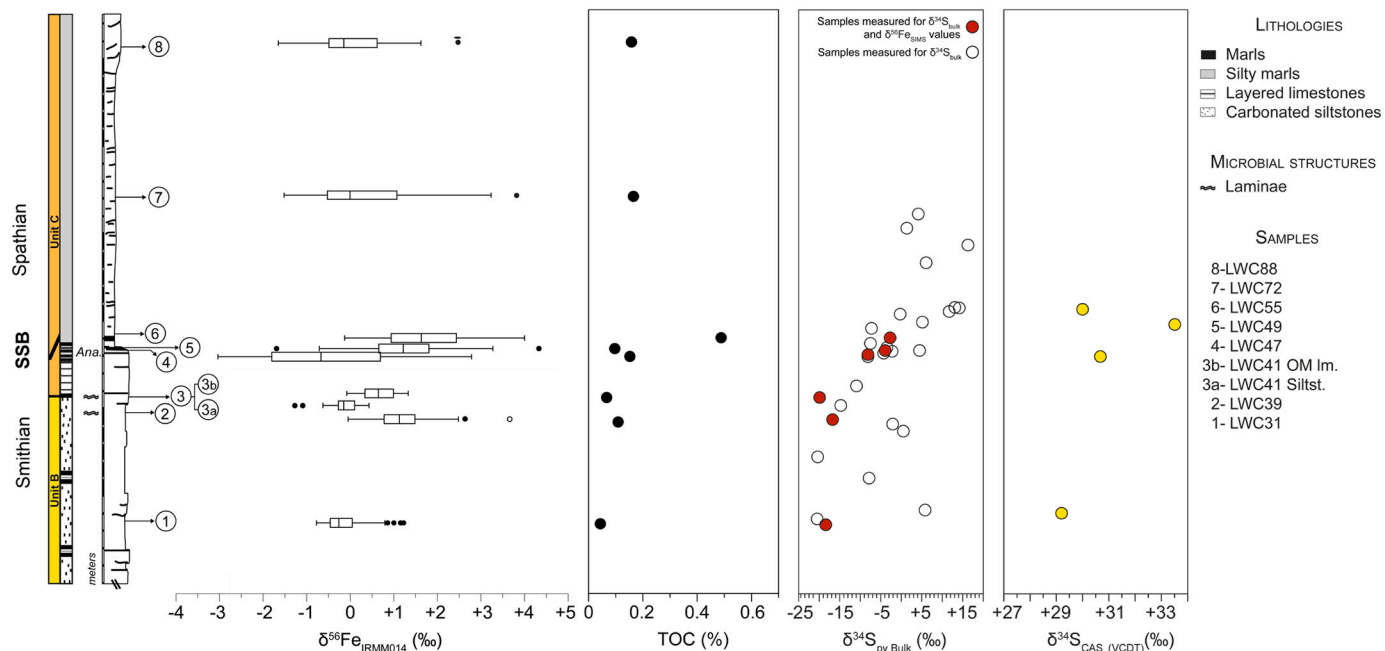


Fig. 3. Evolution of Fe isotope compositions measured by SIMS on 8 LWC samples with corresponding total organic carbon concentrations (in %), pyrite  $\delta^{34}\text{S}$  values on 30 samples (LWC31 to LWC70) and carbonate associated sulfate (CAS)  $\delta^{34}\text{S}$  values on 5 samples of the section. The simplified log reports lithologies and positions of samples measured by SIMS.

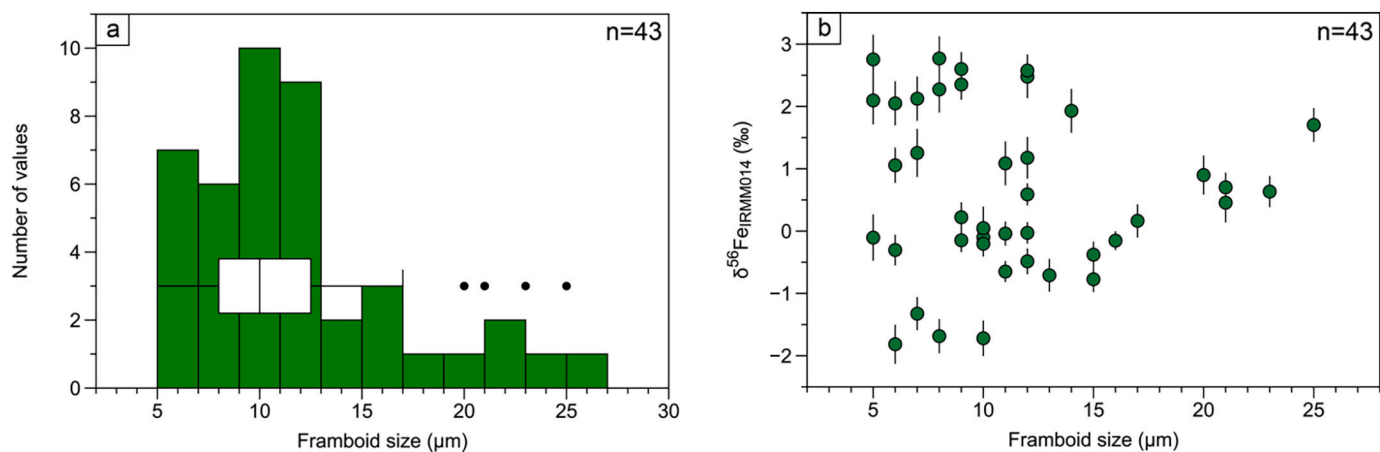
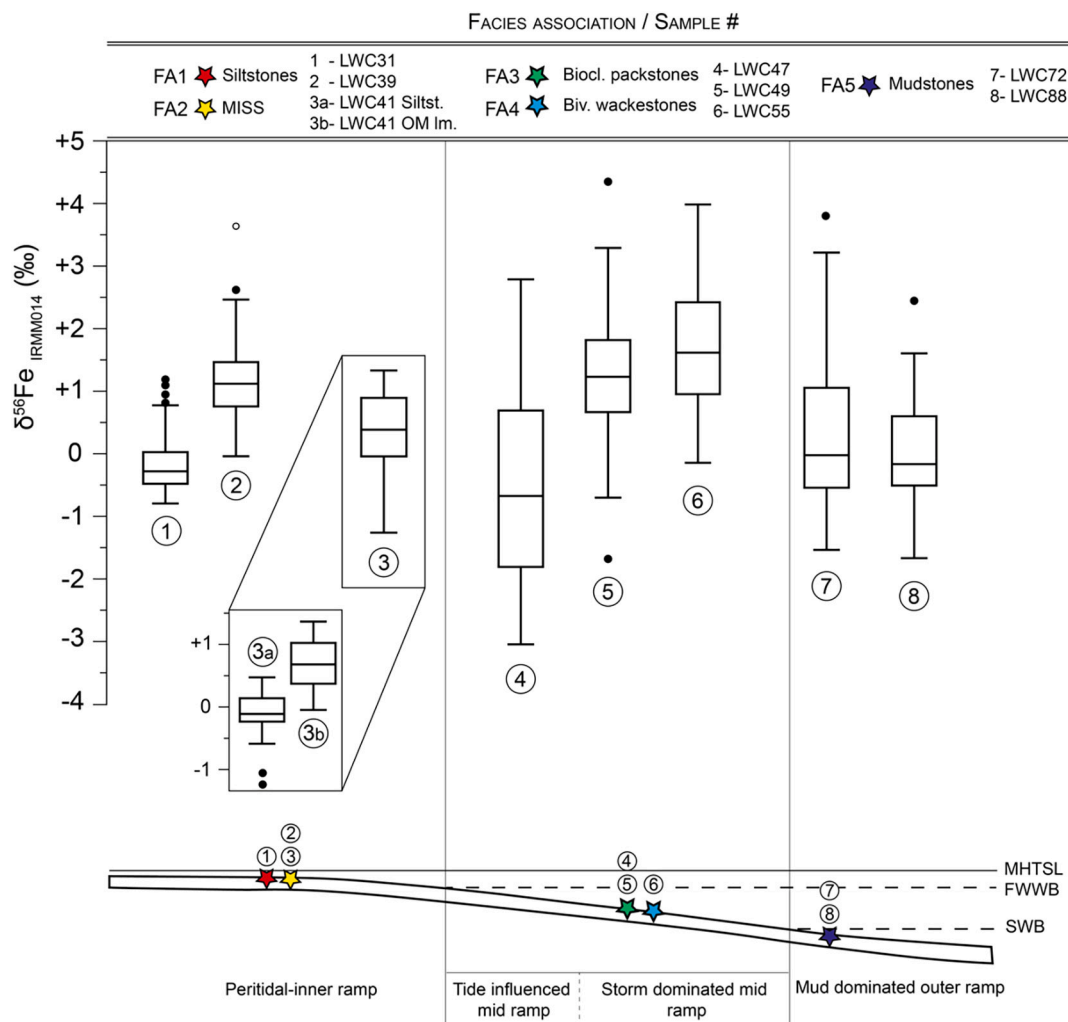


Fig. 4. a) Framboid size distribution (histogram and box plot) of the 43 framboids measured in five LWC samples (LWC47 to LWC88) and b) relationship between the size of framboid pyrite grains and their Fe isotope compositions.



**Fig. 6.** Fe isotope compositions of pyrite from the Lower Weber Canyon section as a function of the depositional environment along a ramp system. The different star colors refer to the corresponding facies associations. Sample LWC31 is part of FA1 (red star). Samples LWC39 and LWC41 are MISS (FA2, yellow star). Please note that sample LWC41 encloses two facies in which pyrite is observed. The first is the silty part (reported as LWC41 Siltst.) and the second is the OM-rich laminae (noted LWC41 OM). F3 (green star) includes samples LWC47 and LWC49. Sample LWC55 is part of FA4 (blue star). Samples LWC72 and LWC88 are included in FA5 (purple star). Fe isotope compositions are reported using outlier box plot representation. Line through the box is the median and the edges of the box represent the quartiles (lower line is the 1st quartile Q1, i.e. the 25th percentile, and upper line is the 3rd quartile Q3, i.e. the 75th percentile). Lower and upper whiskers represent 1.5\*IQR (interquartile range, i.e. the range between Q1 and Q3). The minimum and maximum are marked by small lines at the end of whiskers and represent respectively the lowest and highest values of the distribution, excluding outlier values of the dataset (filled and unfilled dots below and above whiskers). See Fig. 1 for abbreviations. (For interpretation of the references to colour in this figure legend, the reader is referred to the web version of this article.)

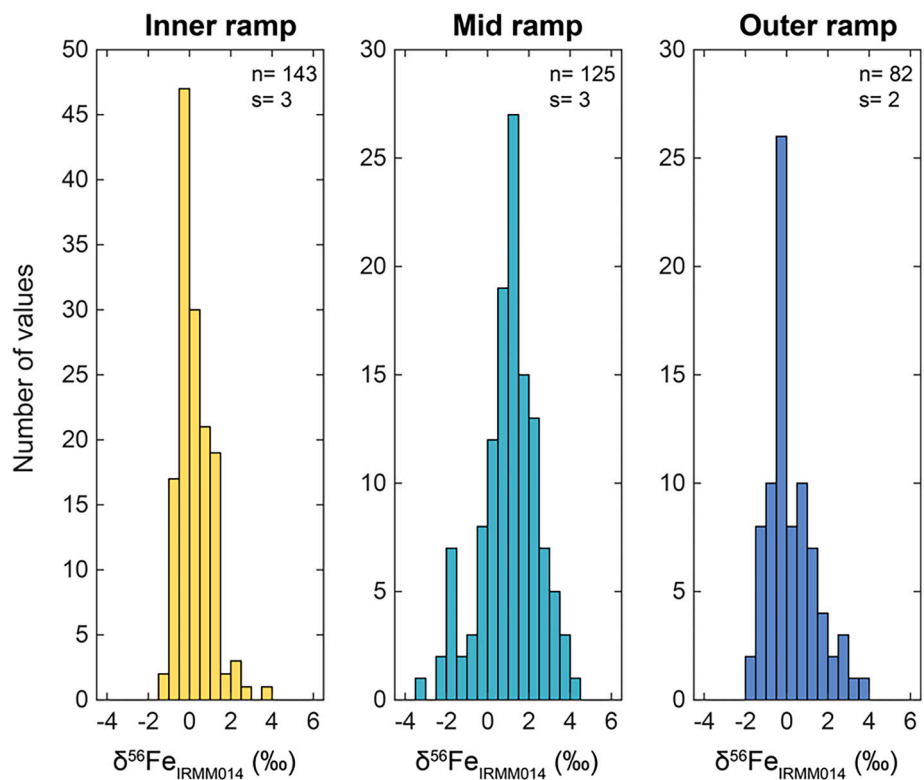


Fig. 7. Pyrite  $\delta^{56}\text{Fe}$  distributions as a function of the domain of the ramp, i.e. the inner ramp, the mid ramp and the outer ramp system. The number of values (n), and the number of samples from which pyrite grains were measured (s) are indicated for each histogram.

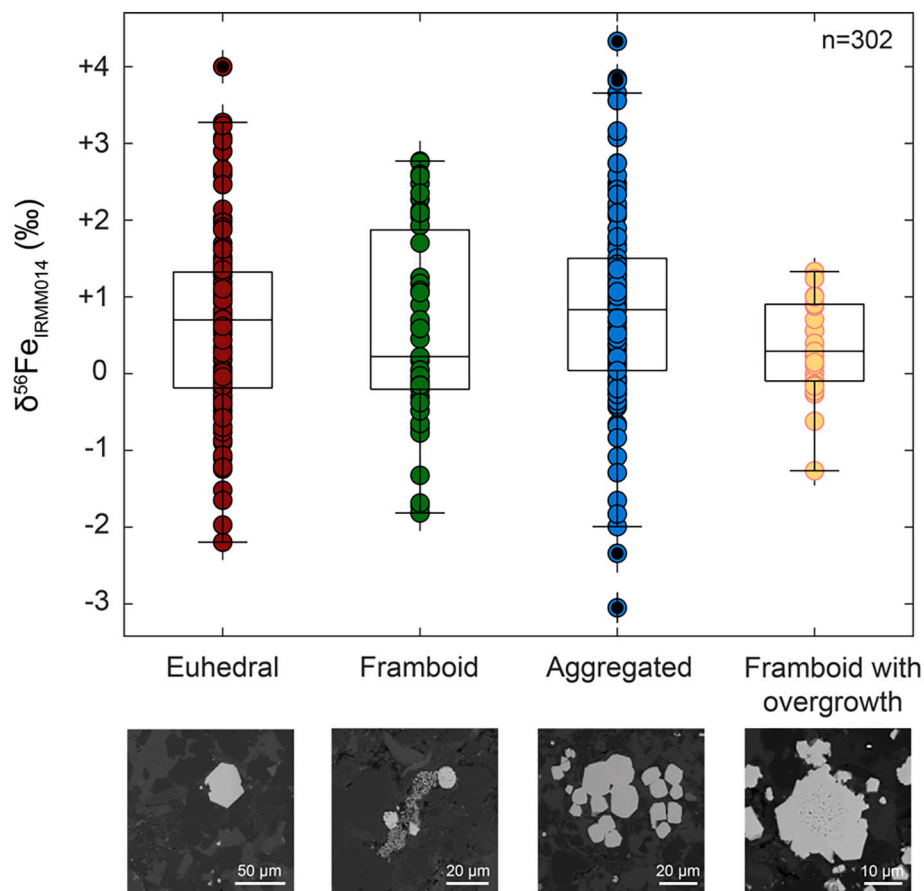
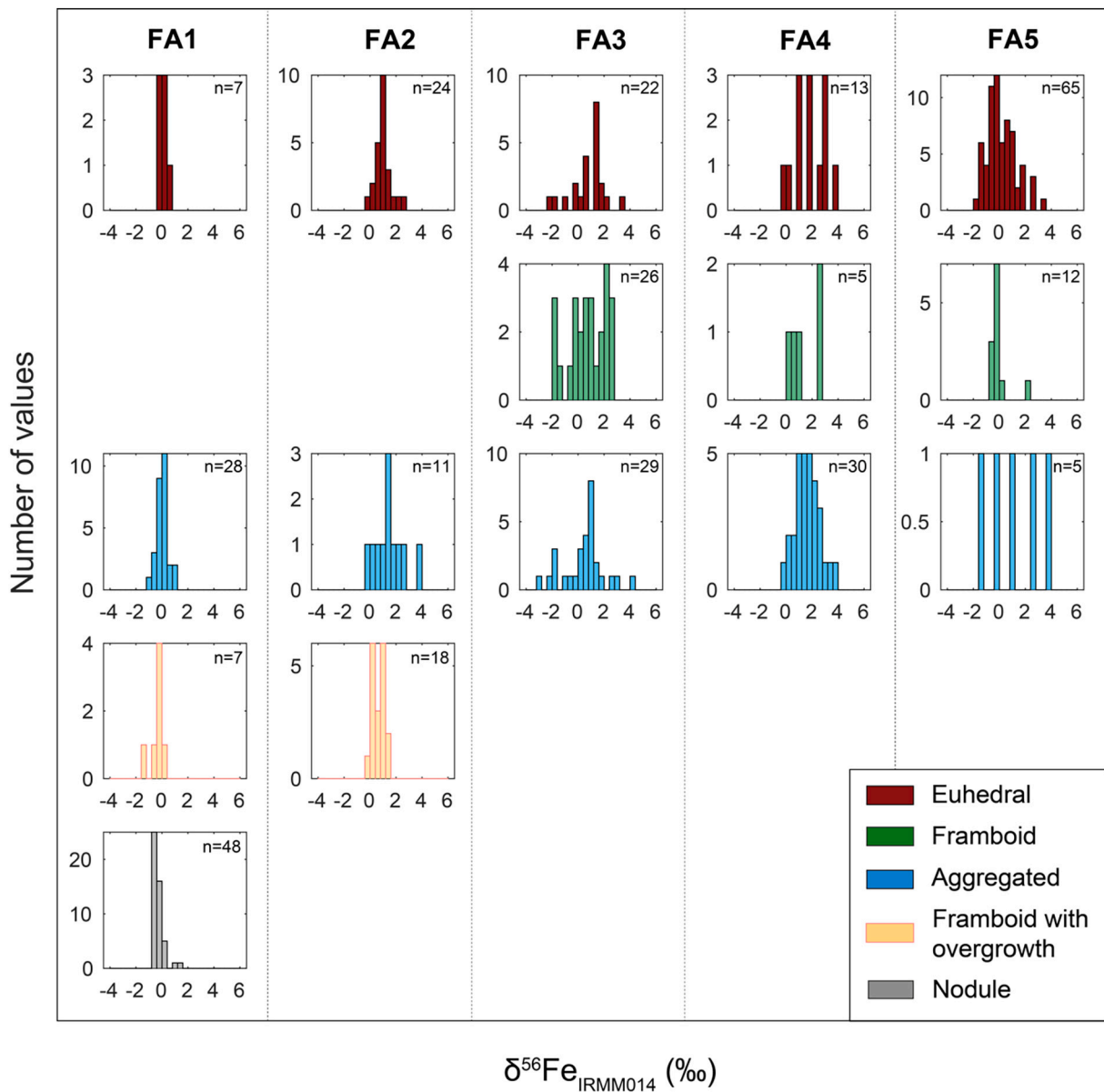
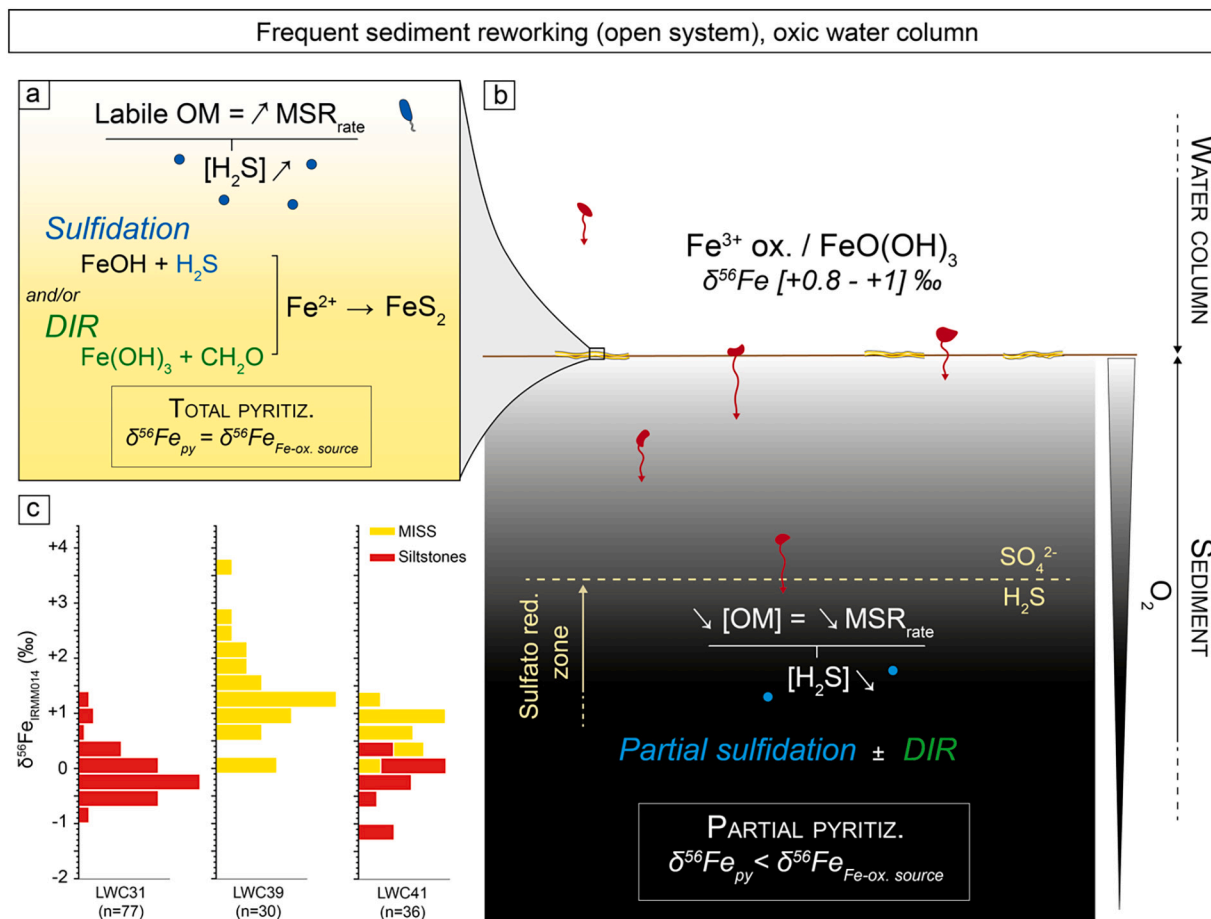


Fig. 8.  $\delta^{56}\text{Fe}_{\text{py}}$  as a function of the morphology of pyrite grains. The different pyrite types are categorized as euhedral, framboids, aggregated and framboids with secondary overgrowth. No statistical differences are observed between each morphology.



**Fig. 9.** Pyrite  $\delta^{56}\text{Fe}$  distributions as a function of pyrite morphologies in each facies (FA1 to FA5). Data from euhedral pyrite are reported in red, from framboids in green, from aggregates in blue, from framboids with secondary rims in yellow and from the nodule in grey. The number of values (n) is indicated for each histogram. (For interpretation of the references to colour in this figure legend, the reader is referred to the web version of this article.)



**Fig. 10.** Iron cycling model in the sediments from inner ramp samples. a) Model of Fe reduction for MISS samples (FA2), where high rate of sulfate reduction promotes the complete conversion of Fe-oxides into Fe<sup>2+</sup> or FeS and subsequently pyrite by reaction with H<sub>2</sub>S (blue pathway: Sulfidation) combined with the possible effect of iron reducing bacteria (green pathway: Dissimilatory Iron Reduction). b) Model of Fe reduction for siltstone samples (FA1). In this model, less abundant and less labile organic matter is available for sulfate reducers, leading to a lower production of H<sub>2</sub>S. In this case, the quantity of H<sub>2</sub>S limits the reduction of Fe-oxides. c) Pyrite  $\delta^{56}\text{Fe}_{py}$  distributions for the facies associations FA1 (siltstone) and FA2 (MISS). (For interpretation of the references to colour in this figure legend, the reader is referred to the web version of this article.)

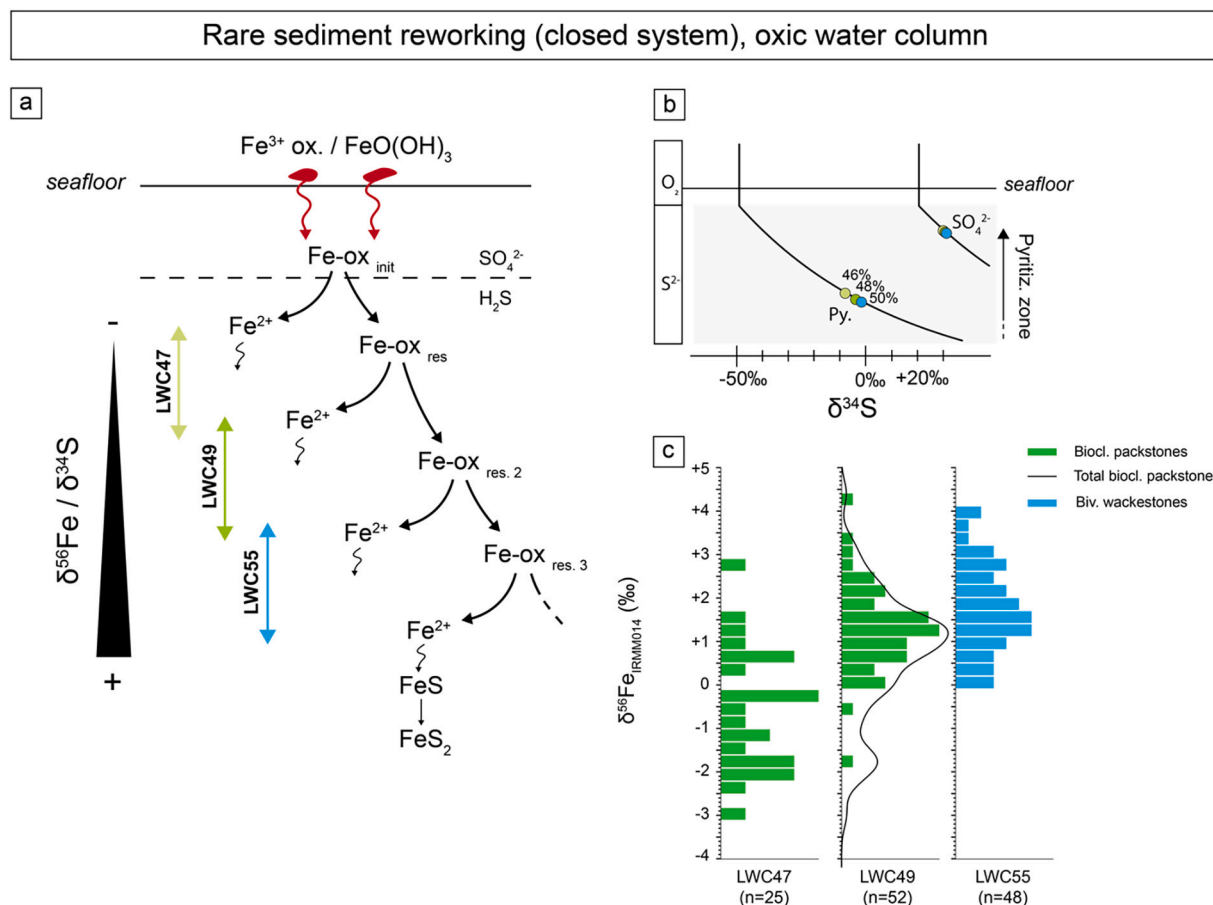


**Fig. 11.** Iron cycling model in the sediments from mid and outer ramp samples. a) Model for Fe-oxide reduction in closed-system, where Fe-oxides are partially reduced by reaction with a restricted amount of  $\text{H}_2\text{S}$  (as sulfate reservoir also evolves in a closed-system), leading to the buildup of different residual Fe-oxide pools. b) Evolution of newly formed pyrite and sulfate in a closed sediment. Percentage of newly formed pyrite during the Rayleigh process is reported for LWC 47 (light green), LWC49 (green) and LWC55 (blue). c) Pyrite  $\delta^{56}\text{Fe}$  distributions for samples from FA3 and FA4. Green and blue colors correspond to facies associations FA3 (bioclastic packstones) and FA4 (bivalve wackestones) respectively. Black line represents probability density for both LWC47 and LWC49. (For interpretation of the references to colour in this figure legend, the reader is referred to the web version of this article.)

iron reducers may have been involved in the reduction of Fe oxides, the newly corrected data are still not sufficiently negative to support dissimilatory iron reduction (DIR) as the dominant reduction pathway (Crosby et al., 2005; corrected Fig. 10c). Instead of a model requiring several oxidation-reduction cycles to explain pyrite  $\delta^{56}\text{Fe}$  values as originally exposed, this new model proposes that the key driver of pyrite formation is the sulfidation of Fe oxides by microbial  $\text{H}_2\text{S}$ , the production of which depends on the sedimentary facies.

#### Acknowledgments

The authors would like to thank the Origin Laboratory at the University of Chicago, Dr. Rego, and Prof. Dauphas for their analyses of the Balmat-UNIL standard that led to the discovery of this error.

#### Appendix A. Supplementary data

Supplementary data to this article can be found online at <https://doi.org/10.1016/j.palaeo.2023.111636>.

#### References

Crosby, H.A., Johnson, C.M., Roden, E.E., Beard, B.L., 2005. Coupled Fe(II)-Fe(III) Electron and Atom Exchange as a Mechanism for Fe Isotope Fractionation during

- Dissimilatory Iron Oxide Reduction. *Environ. Sci. Technol.* 39, 6698–6704. <https://doi.org/10.1021/es0505346>.
- Dauphas, N., Rouxel, O., 2006. Mass spectrometry and natural variations of iron isotopes. *Mass Spectrom. Rev.* 25 (4), 515–550. <https://doi.org/10.1002/mas.20078>.
- Dauwe, B., Middelburg, J.J., Herman, P.M., Heip, C.H., 1999. Linking diagenetic alteration of amino acids and bulk organic matter reactivity. *Limnol.* 44, 1809–1814.
- Marin-Carbonne, J., Rollion-Bard, C., Luais, B., 2011. In-situ measurements of iron isotopes by SIMS: MC-ICP-MS intercalibration and application to a magnetite crystal from the Gunflint chert. *Chem. Geol.* 285 (1–4), 50–61. <https://doi.org/10.1016/j.chemgeo.2011.02.019>.
- Meister, P., Liu, B., Ferdelman, T.G., Jørgensen, B.B., Khalili, A., 2013. Control of sulphate and methane distributions in marine sediments by organic matter reactivity. *Geochim. Cosmochim. Acta* 104, 183–193. <https://doi.org/10.1016/j.gca.2012.11.011>.
- Middelburg, J.J., 1989. A simple rate model for organic matter decomposition in marine sediments. *Geochim. Cosmochim. Acta* 53, 1577–1581. [https://doi.org/10.1016/0016-7037\(89\)90239-1](https://doi.org/10.1016/0016-7037(89)90239-1).
- Rouxel, O.J., Bekker, A., Edwards, K.J., 2005. Iron isotope constraints on the archaic and paleoproterozoic ocean redox state. *Science* 307, 1088–1091. <https://doi.org/10.1126/science.1105692>.
- Whitehouse, M.J., Fedo, C.M., 2007. Microscale heterogeneity of Fe isotopes in > 3.71 Ga banded iron formation from the Isua Greenstone Belt, Southwest Greenland. *Geology* 35 (8), 719–722. <https://doi.org/10.1130/G23582A.1>.
- Wu, L., Beard, B.L., Roden, E.E., Johnson, C.M., 2011. Stable iron isotope fractionation between aqueous Fe(II) and hydrous ferric oxide. *Environ. Sci. Technol.* 45, 1847–1852. <https://doi.org/10.1021/es103171x>.
- Xu, L., Yang, J.H., Xie, L.W., Wang, H., Yang, Y.H., Huang, C., Wu, S.T., 2022. Evaluation of plasma condition, concentration effect, position effect, and nickel-doping method on non-matrix-matched Fe isotopic analysis by femtosecond laser ablation multi-collector inductively coupled plasma mass spectrometry. *Spectrochim. Acta Part B Atom. Spectros.* 189, 106374. <https://doi.org/10.1016/j.sab.2022.106374>.